

## Supporting Information

### Electrochemical Synthesis to Convert Ag Film into Ag Nanoflowers with High Electrocatalytic Activity

Ya-Huei Chang,<sup>‡a</sup> Chang Liu,<sup>‡a</sup> Sergei Rouvimov,<sup>b</sup> Tengfei Luo<sup>c</sup> and Shien-Ping Feng<sup>\*a, d</sup>

### Experimental Section

**Synthesis of Ag NCs.** All electrochemical synthesis was conducted with CHI 660E in a standard three-electrode system with Ag-coated FTO as the working electrode, Pt mesh as the counter electrode, and saturated Ag/AgCl as the reference electrode. The clean substrates of fluorine-doped tin oxide conductive glass (1 cm × 1.5 cm; 8 Ω/□) were immersed in 1 v/v% 3-mercaptopropyl-trimethoxysilane in ethanol for 3 min at room temperature for the formation of self-assembled monolayers. An intact Ag layer (150 nm) was then electroplated onto the MPS-grafted FTO in a commercial silver electrolyte (Metaler MetSil 500CNF R-T-U; contents, 0.28 M of Ag ions, cyanide free) at room temperature. To synthesize Ag NCs, Ag-coated substrate was subjected to CSE in a weak alkaline electrolyte consisting of 0.312 M CH<sub>3</sub>COONa, 0.078 M NiSO<sub>4</sub>, and 0.1 M Na<sub>2</sub>SO<sub>4</sub> at room temperature. For the synthesis of the flower-like Ag NCs, the potential swept from 0 to 1.2 V (anodic stripping) and then back from 1.2 to 0 V at 10 mV/s (reduction process), which can be completed within 4 minutes. Icosahedral and decahedral Ag NCs were produced by the same forward scan and a modified reversed scan from 1.2 V to 0.3 V with a high scan rate of 50 mV/s. For the synthesis of Ag nanorods, a square-wave form was applied ( $E_{\text{on}} = 0.3$  V,  $E_{\text{off}} = 0.9$  V; 10 Hz) for 10 min

after anodic stripping. The Ag dendrites was produced by changing the potential range in the square-wave form ( $E_{\text{on},1} = 0.3 \text{ V}$ ,  $E_{\text{on},2} = 0 \text{ V}$ ; 10 Hz) for 10 min. As noted, the forward anodic scan is only used to create  $\text{Ag}^+$  and  $\text{Ni}^{3+}$  in the solution, and the scan rate is adjustable.

***Material and electrochemical characterizations.*** The synthetic Ag NCs were directly characterized with a field-emission scanning electron microscope (Hitachi S-4800) and a high-resolution TEM (Tecnai, G220S-Twin). The CVs of flower-like Ag NCs/FTO were carried out in the 0.1 M NaOH electrolyte with glucose levels ranging from 0 to 500  $\mu\text{M}$ . Before amperometric measurement, an anodic scan from 0 V to 1.2 V at a scan rate of 10 mV/s was performed in 0.1 M NaOH as a pre-treatment. The amperometric responses of flower-like Ag NCs/FTO to glucose with different concentrations ranging from 0.1 nM to 100  $\mu\text{M}$  were recorded at a potential of 0.95 V under stirring conditions. Successive addition of glucose into 0.1 M NaOH was performed with a computer-controlled dispensing machine (Sindatek 100 SB) to ensure the precision of the concentrations. In order to keep a constant active area for the electro-oxidation of glucose, the upper belt (2 mm) of flower-like Ag NCs/FTO electrode was taped (the black tape shown in Supporting video S1).

## Supplementary Figures

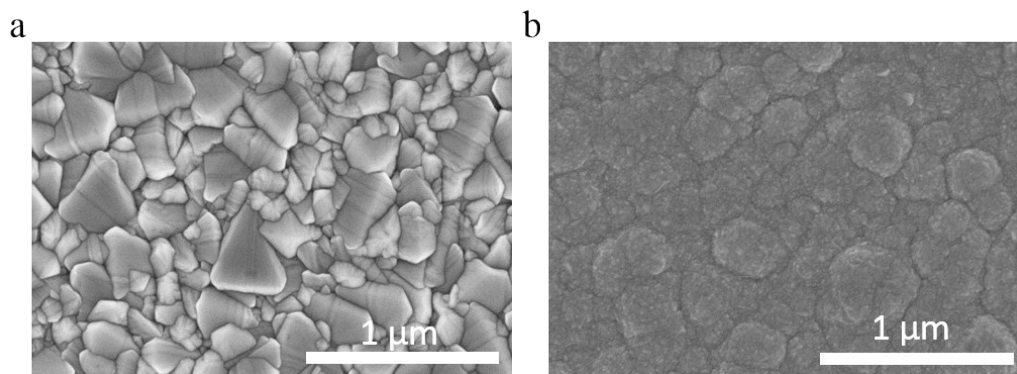


Fig. S1 SEM images of (a) FTO pretreated with MPS and (b) electroplated Ag layer on MPS-grafted FTO.

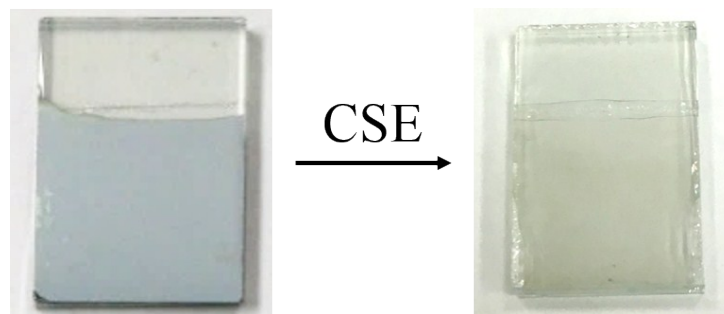


Fig. S2 Appearance of FTO substrate changes from shiny Ag-coated surface to semitransparent surface after CSE.

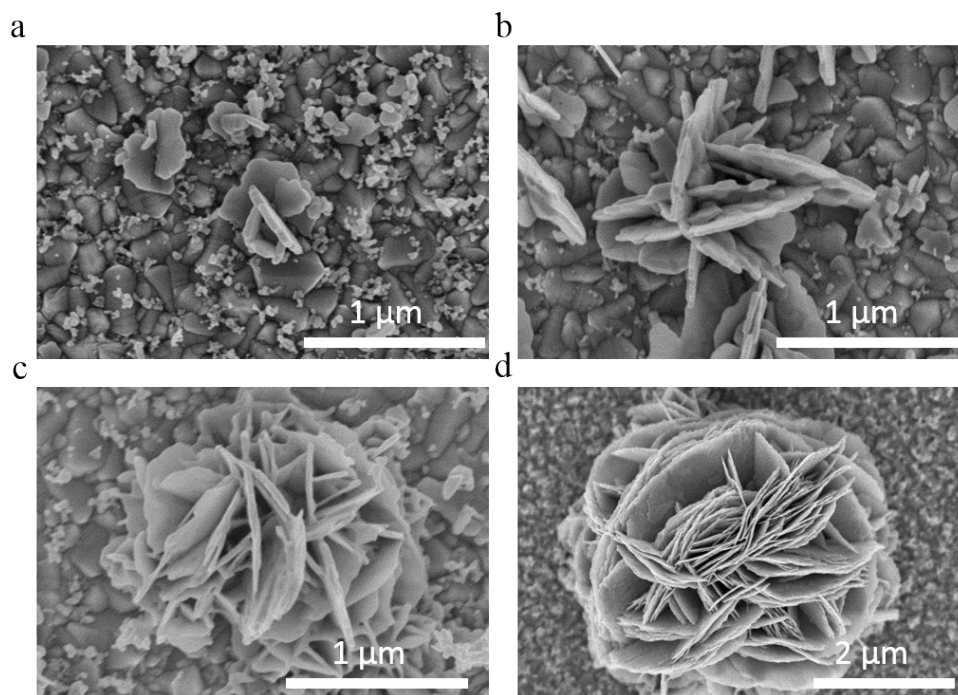


Fig. S3 SEM images of flower-like Ag NCs on FTO via CSE under different end points of reversed scan at (a) 0.35 V, (b) 0.3 V, (c) 0.2 V, and (d) 0 V.

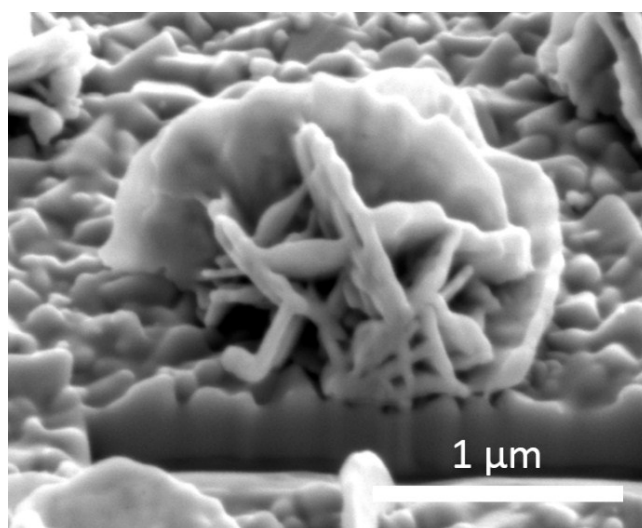


Fig. S4 Cross-sectional view of flower-like Ag NCs. (Sample was prepared by using focused ion beam to cut edge of flower-like Ag NCs perpendicularly).

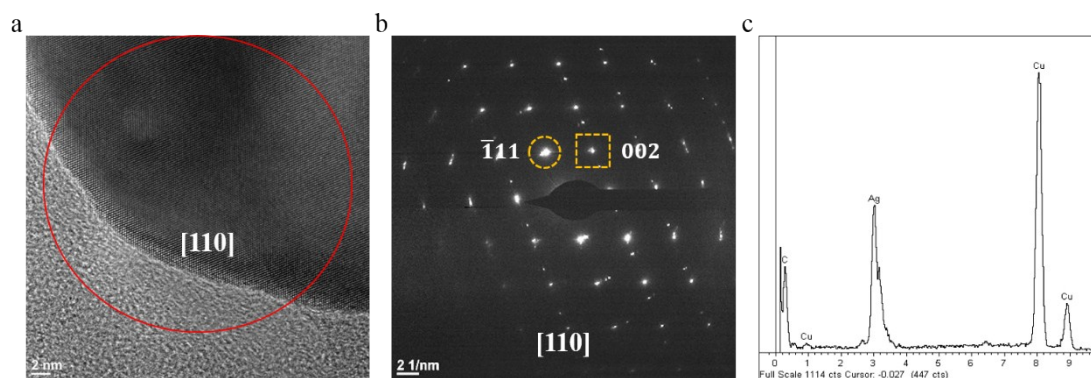


Fig. S5 (a) HR-TEM image and (b) SAED pattern for side-plane of one nanopetal tilted at  $34.8^\circ$  along the  $[110]$  zone axis.  $\{111\}$  and  $\{002\}$  Bragg reflections are marked by circle and box spots, respectively. (c) Energy-dispersive X-ray (EDX) spectrum of flower-like Ag NCs on TEM Cu grids. (The C and Cu signals originated from TEM grids.)

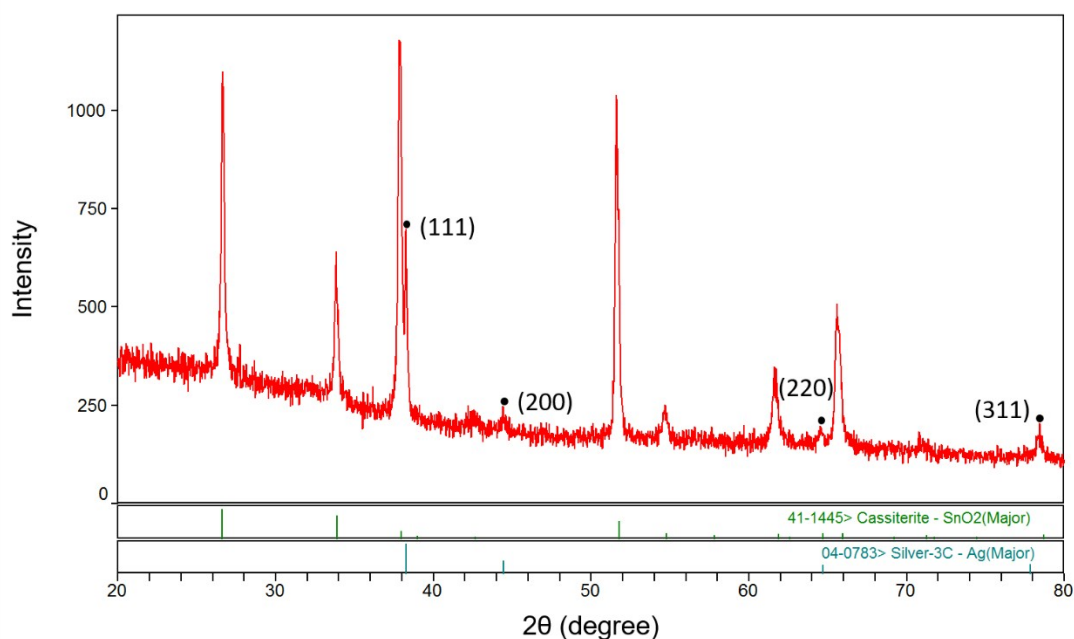


Fig. R6 XRD pattern of flower-like Ag NCs on FTO substrate. XRD peaks at  $2\theta$  of  $38^\circ$ ,  $44^\circ$ ,  $64^\circ$  and  $77^\circ$  can be attributed to  $\{111\}$ ,  $\{200\}$ ,  $\{220\}$  and  $\{311\}$  crystallographic planes of the FCC Ag crystals with the ratio of  $7 : 2.5 : 2 : 2$ , respectively.

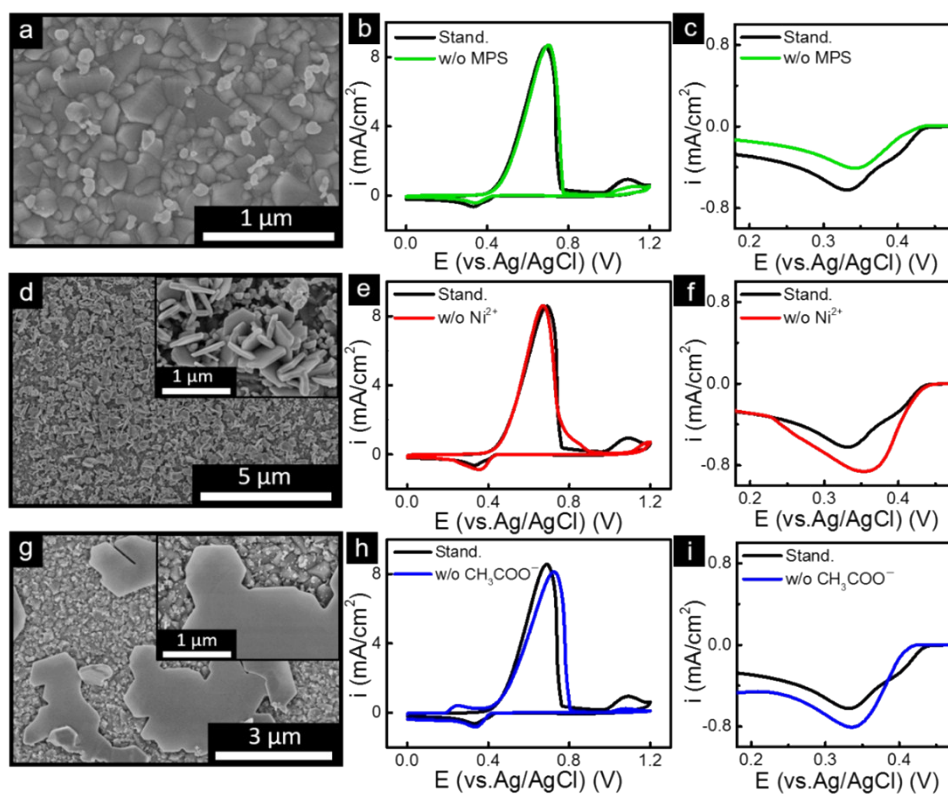


Fig. S7 SEM images, current-potential responses and cathodic curves of Ag NCs in the condition of (a-c) without MPS pretreatment, (d-f) without Ni<sup>2+</sup> in the electrolyte, (g-i) without CH<sub>3</sub>COO<sup>-</sup> in the electrolyte.

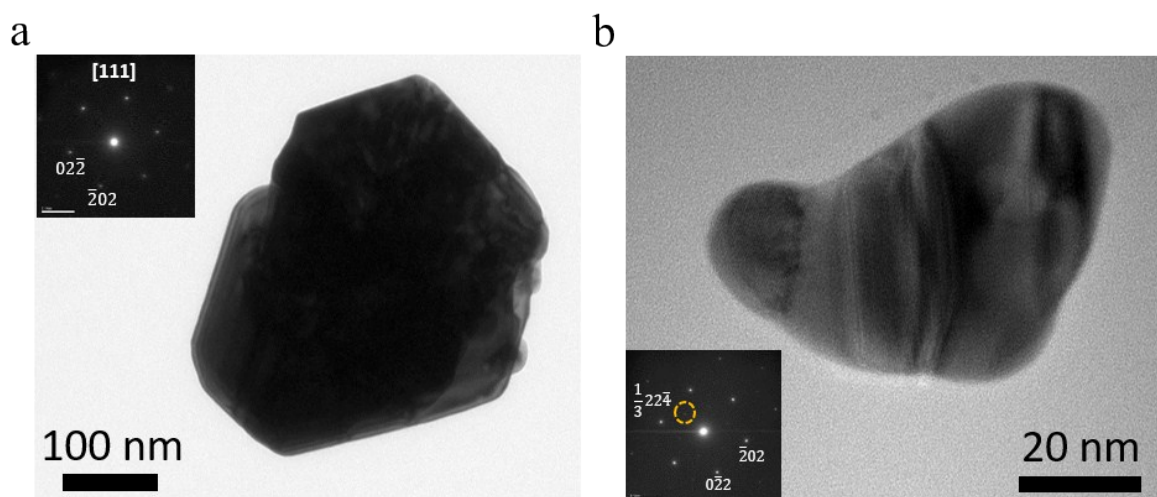


Fig. S8 TEM image for one nanopetal of flower-like Ag NCs via CSE in (a) electrolyte without Ni<sup>2+</sup> ions and (b) standard electrolyte. Insets are corresponding SAED.

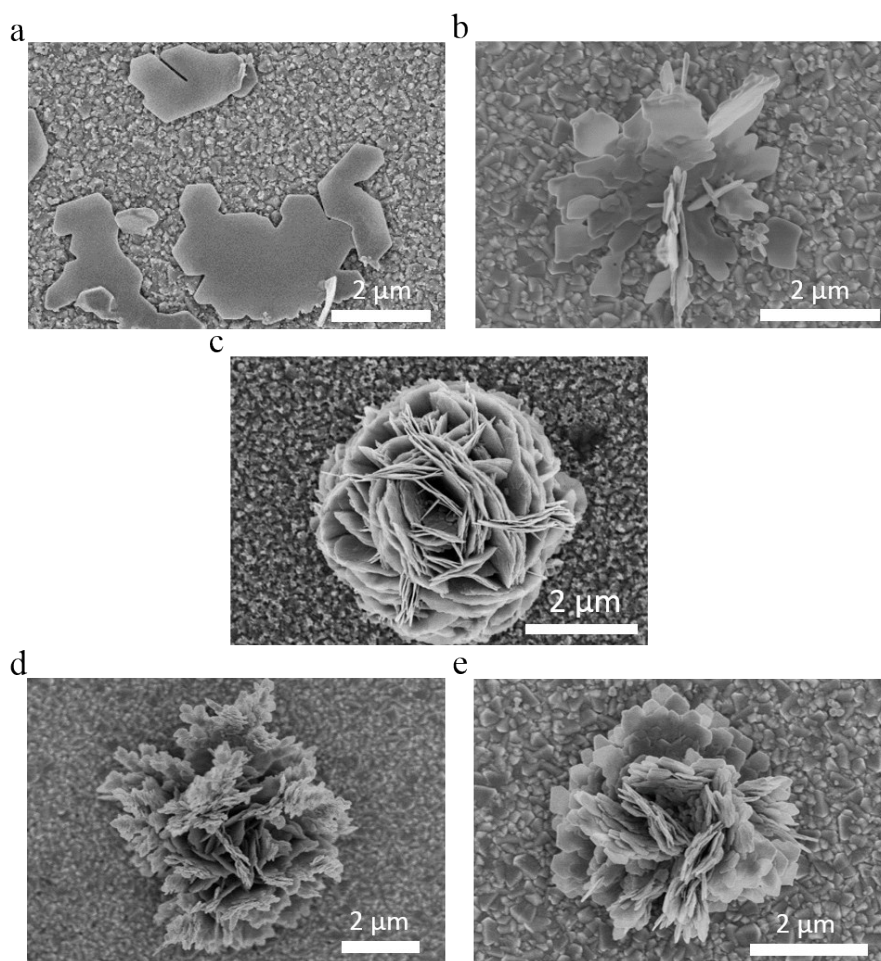


Fig. S9 SEM images for morphological change of Ag NCs with different ratios of  $[\text{CH}_3\text{COO}^-]/[\text{SO}_4^{2-}]$  in electrolyte under the same CSE condition. Experimental conditions are listed in Table S1.

Table S1. Electrolyte compositions for the formation of Ag NCs via CSE. The concentration of  $\text{Ni}^{2+}$  ions is 0.178 M for each condition. Ac represents acetate ( $\text{CH}_3\text{COO}^-$ ).

Electrolyte Composition				Anion Concentration		Ratio	pH	Figure
$\text{NiSO}_4$ (M)	NaAc (M)	$\text{Na}_2\text{SO}_4$ (M)	$\text{NiAc}_2$ (M)	$\text{SO}_4^{2-}$ (M)	$\text{CH}_3\text{COO}^-$ (M)	$[\text{CH}_3\text{COO}^-]/$ $[\text{SO}_4^{2-}]$		
0.078	-	0.1	-	0.178	0	0	6.17	S9 (a)
0.078	0.312	0.15	-	0.228	0.312	1.4	7.17	S9 (b)
0.078	0.312	0.1	-	0.178	0.312	1.8	7.01	S9 (c)
0.078	0.624	0.1	-	0.178	0.624	3.5	7.47	S9 (d)
-	0.312	-	0.078	0	0.468	$\infty$	7.41	S9 (e)

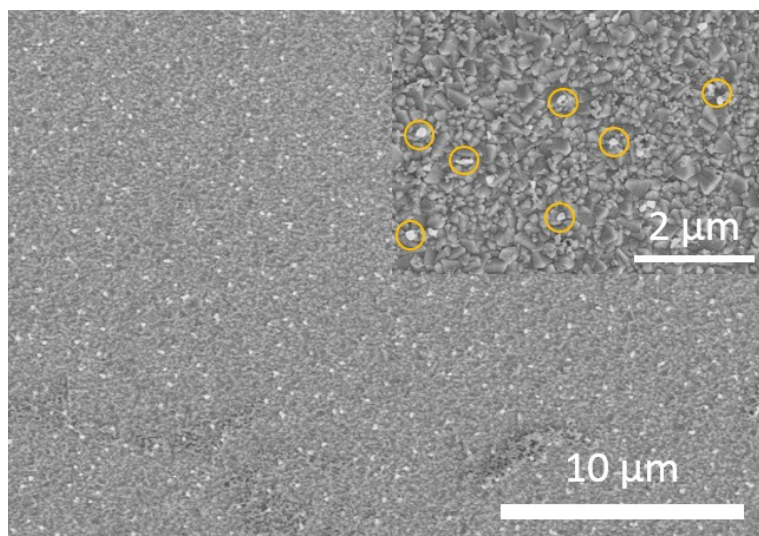


Fig. S10 SEM images for Ag layer coated on MPS-grafted FTO after CSE in electrolyte without  $\text{SO}_4^{2-}$  ions. Inset shows remaining Ag islands on FTO (marked by orange circles).

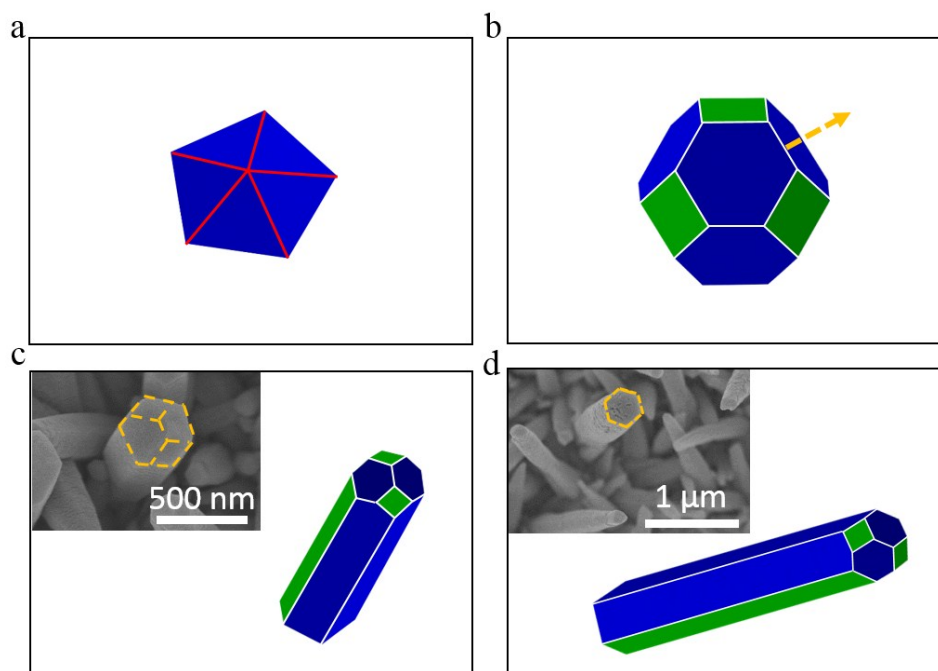


Fig. S11 Schematic illustration of the evolution pathway from (a) decahedral Ag seed to (b) a truncated octahedral Ag NC, and then to (c) and (d) Ag nanorods with hexagonal cross section on the top. The yellow arrow indicates one possible growth direction of the truncated octahedral Ag NC. The blue and green colors represent the  $\{111\}$  and  $\{100\}$  facets, respectively. Twin planes are delineated in the drawing with red lines. The insets of (c) and (d) are SEM images of Ag nanorods.

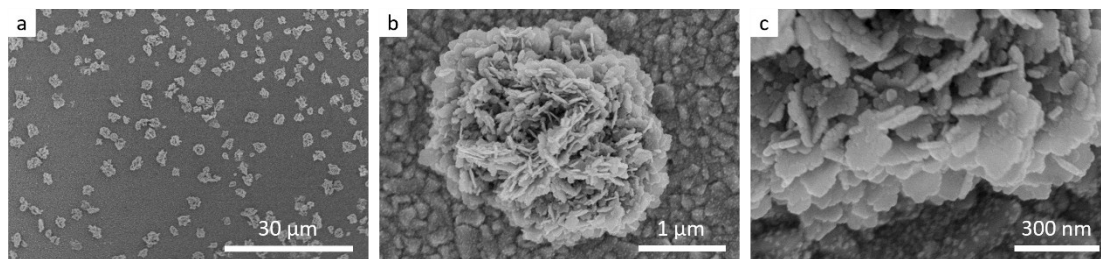


Fig. S12 SEM images of flower-like Ag NCs on FTO via 5 CSE cycles under different magnifications.

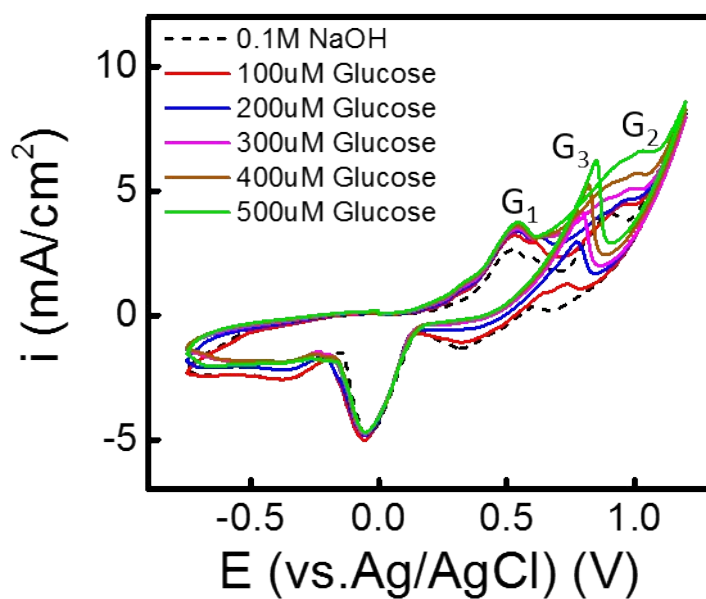
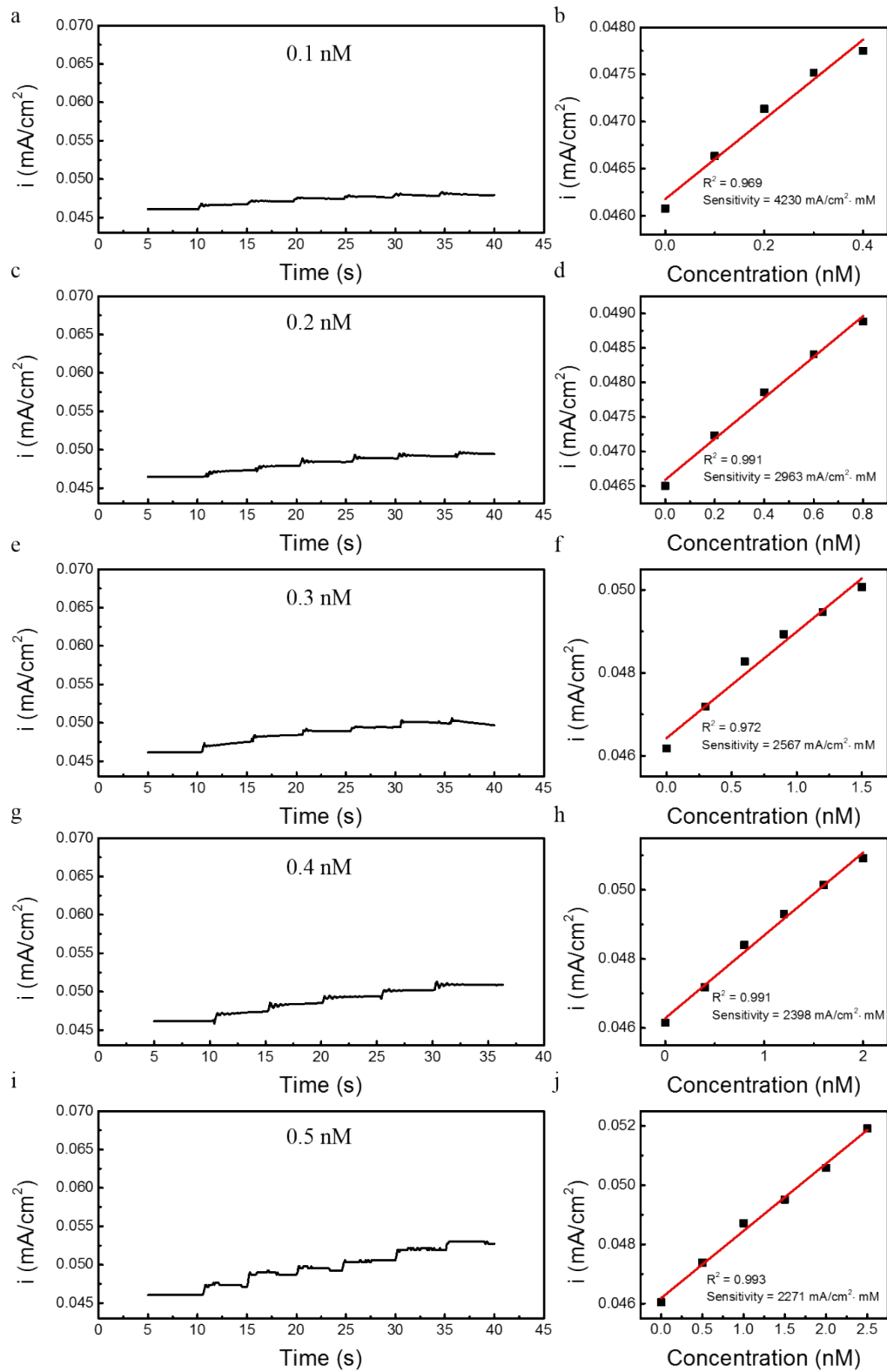


Fig. S13 Cyclic voltammograms of flower-like Ag NCs/FTO electrode with and without glucose in 0.1 M NaOH



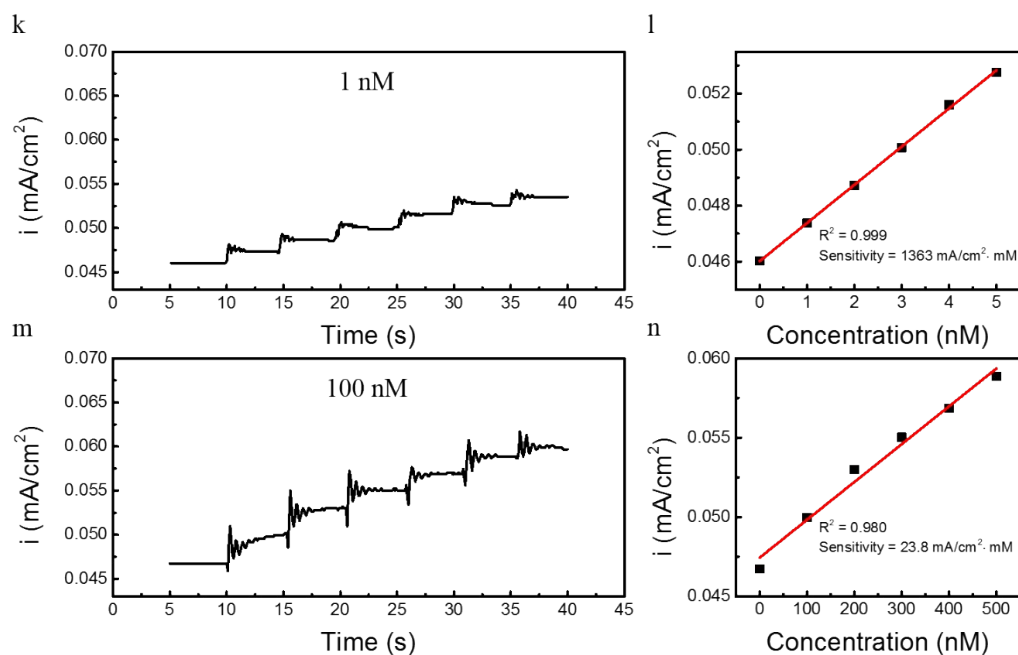


Fig. S14 Amperometric response and glucose sensitivity of flower-like Ag NCs/FTO electrode in stirred 0.1 M NaOH at different concentrations of added glucose: (a, b) 0.1 nM, (c, d) 0.2 nM, (e, f) 0.3 nM, (g, h) 0.4 nM, (i, j) 0.5 nM, (k, l) 1 nM, and (m, n) 100 nM under operating potential of 0.95 V.

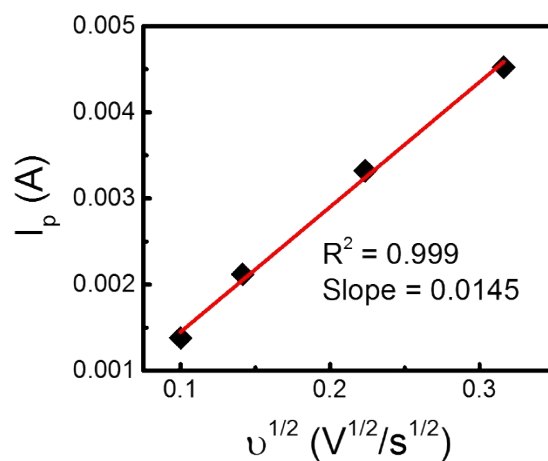


Fig. S15 Plot of peak current versus the square root of potential scan rate with an auxiliary linear fit in ferro/ferricyanide redox system.

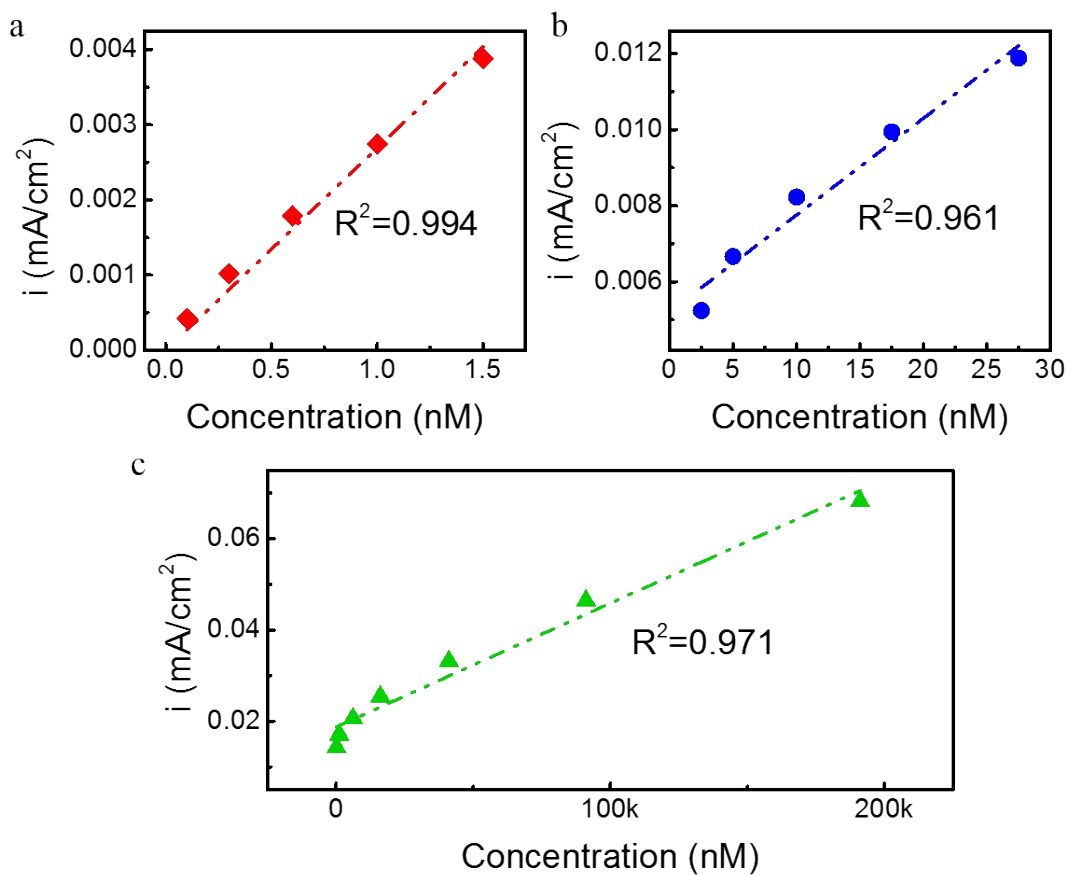


Fig. S16 Linear calibration plots (current density versus glucose concentration) of flower-like Ag NCs/FTO electrode for different linear detection ranges at (a) 0.1 nM to 0.5 nM, (b) 1 nM to 10 nM and (c) 100 nM to 100  $\mu\text{M}$ .

## Supplementary Notes

### **Supplementary Note 1: Galvanic Ostwald ripening for further growth in the diameter of flower-like Ag NCs**

The large Ag NC has a greater work function, resulting in a more negative charge than the tiny one at electrical equilibrium; therefore, the size difference between Ag NCs causes different standard electrode potentials. When Ag NCs are connected by a conductive substrate in the electrolyte, the larger Ag NCs accept electrons from the neighboring smaller Ag NCs through the FTO, and the smaller Ag NCs reestablish equilibrium by dissolving  $\text{Ag}^+$  into the electrolyte (galvanic Ostwald ripening).<sup>1</sup> As shown in Fig. S3c for the end point of 0.2 V in the reversed cathodic scan, the Ag flower with a diameter of 1.5  $\mu\text{m}$  is surrounded by tiny Ag nanoplatelets. The galvanic Ostwald ripening effect would induce the consumption of tiny Ag nanoplatelets to further grow in the diameter of Ag flowers ( $\sim 3 \mu\text{m}$ ) during the potential between 0.2 V and 0 V (end point of 0V), as shown in Fig. S3d.

### **Supplementary Note 2: Pre-formation of thin metal film incorporating with MPS**

Fig. S7a shows the presence of only a small number of scattered nanoparticles after CSE when using Ag coated on bare FTO. Our previous study showed that MPS provides a strong covalent bond to improve the nucleation process and the interfacial contact between the electroplated metal and substrate.<sup>2, 3</sup> In this case, it is believed that the MPS layer remained on the FTO surface after anodic stripping and therefore served as an effective bridging-link layer to promote electroplating nucleation at the reversed

cathodic potential. Fig. S7b shows the current-potential response for the Ag coated on bare and MPS-grafted FTO under the same CSE. The similar peak  $A_1$  indicates the same anodic stripping process for the bare and MPS-grafted samples. The corresponding cathodic curves in Fig. S7c show a smaller peak  $C_1/C_2$  for the bare sample than for the MPS-grafted sample, which demonstrates the efficacy of MPS as a promoter of nucleation.

### **Supplementary Note 3: The roles of electrolyte medium — $Ni^{2+}$ ions**

In the absence of  $Ni^{2+}$  ions shown in Fig. S7d, a large amount of Ag clusters with standing intercrossed hexagonal nanoplates were obtained on MPS-grafted FTO after CSE. It has been reported that two-dimensional growth along the side planes of the  $\{111\}$  facet favors a hexagonal shape to minimize the total surface energy.<sup>4</sup> The six-fold symmetry of the diffraction spots for one of the hexagonal nanoplates indicates that the hexagonal faces are bound by  $\{111\}$  planes (Fig. S8a) and that their side faces must be bound by a mixture of  $\{100\}$  and  $\{111\}$  planes.<sup>5</sup> To compare the red curve with the black curve (Fig. S7e), the absence of  $Ni^{2+}$  does not influence Ag stripping, which results in a similar peak  $A_1$  while causing a disappearance of peak  $A_2$  due to the lack of electro-oxidation of  $Ni^{2+}/Ni^{3+}$ . In the presence of  $Ni^{2+}$ , we found that the  $Ni^{3+}$  produced by electro-oxidation of  $Ni^{2+}$  at peak  $A_2$  would act as an etchant during the formation of Ag NCs. When the Ag clusters and  $Ni^{3+}$  co-exist in the system,  $Ni^{3+}$  is preferentially reduced to  $Ni^{2+}$  and Ag is dissolved into  $Ag^+$ . The corresponding cathodic curves in Fig. S7f show that these simultaneous reduction and oxidation reactions

decrease the overall cathodic current response; therefore, the black curve has a smaller current response at peaks  $C_1$  and  $C_2$  than the red curve. Therefore,  $\text{Ag}^+$  was initially electroplated to form Ag clusters with favored hexagonal nanoplates, and their edge and basal planes were then etched by  $\text{Ni}^{3+}$ , resulting in round Ag nanosheets (Fig. S8b).<sup>6</sup>

#### **Supplementary Note 4: The roles of electrolyte medium — $\text{CH}_3\text{COO}^-$ and $\text{SO}_4^{2-}$ ions**

Fig. S7g shows that only the large flat Ag sheets were electroplated on MPS-grafted FTO without the addition of  $\text{CH}_3\text{COONa}$ , indicating that  $\text{CH}_3\text{COO}^-$  ions play an important role in the formation of the standing-type Ag clusters. The anions are usually used for selective adsorption on certain crystal planes, blocking or slowing their growth to produce high-aspect-ratio NCs.<sup>7</sup>  $\text{SO}_4^{2-}$  and  $\text{CH}_3\text{COO}^-$  are the two types of anions in our electrolyte. The geometric symmetry of  $\text{SO}_4^{2-}$  ( $C_{3v}$ ) prefers to adhere to the Ag  $\{111\}$  plane, whereas that of  $\text{CH}_3\text{COO}^-$  ions have a similar binding affinity for  $\{111\}$  and  $\{100\}$  planes.<sup>8</sup> As mentioned, the basal planes of Ag petal are  $\{111\}$ , and the side planes are a mixture of  $\{100\}$  and  $\{111\}$  planes; therefore, the absence of  $\text{CH}_3\text{COO}^-$  indicates no blocking effect on  $\{100\}$ , leading to rapid growth along the side planes to form flat Ag sheets. Fig. S9 shows the morphological changes of Ag NCs with different ratios of  $[\text{CH}_3\text{COO}^-]/[\text{SO}_4^{2-}]$  in the electrolyte under the same CSE conditions, and the experimental conditions are listed in Table S1. When the  $[\text{CH}_3\text{COO}^-]/[\text{SO}_4^{2-}]$  ratio increases, the size and aspect-ratio of the individual Ag nanopetals decreases and the

number of standing Ag nanopetals increases. To replace  $\text{NiSO}_4$  with  $\text{CH}_3\text{COONi}$ , the flower-like Ag NCs can still be formed without the existence of  $\text{SO}_4^{2-}$ , but the petal sizes became smaller (Fig. S9e). It was found that  $\text{SO}_4^{2-}$  not only acts as a capping agent on  $\{111\}$  planes but also acts as an essential ligand for Ag stripping. The lack of  $\text{SO}_4^{2-}$  causes incomplete Ag stripping, which results in Ag islands remaining on the substrate (Fig. S10). The optimum ratio of  $[\text{CH}_3\text{COO}^-]/[\text{SO}_4^{2-}]$  approximately 2 was observed to produce japonica-like Ag flowers constructed of high-aspect-ratio Ag nanopetals, which were grown from the substrate to the tip continuously. Besides,  $\text{CH}_3\text{COO}^-$  coordinates with metal ions to form  $\text{CH}_3\text{COO-Ni}$  or  $\text{CH}_3\text{COO-Ag}$  complexes in the electrolyte because of the strong chelating ability of carboxyl.<sup>9</sup> Without the formation of the  $\text{CH}_3\text{COO-Ni}$  complex, nickel hydroxide will be formed before Ag stripping, which causes an additional peak ranging from 0.2 to 0.35 V in the blue curve of Fig. S7h. The corresponding cathodic curves of Fig. S7i show that the reduction of Ag ions occurs at a more negative onset voltage in the absence of  $\text{CH}_3\text{COO}^-$  ions because the  $\text{CH}_3\text{COO-Ag}$  complex forms hydrogen bonds to the substrate to reduce the formation energy in the early stage of electroplating.<sup>10</sup>

### **Supplementary Note 5: Electrocatalytic activity of glucose at flower-like Ag NCs/FTO electrode**

Non-enzymatic electrochemical glucose biosensor has been developed to detect glucose based on direct oxidation of glucose on platinum-based, carbon-based or metal oxide based electrode.<sup>11</sup> Song et al. reported the inverse-opal Pt-film with a detection

limit of 0.1  $\mu\text{M}$  for electrochemical glucose detection.<sup>12</sup> In addition to noble metal electrode, the composite material of nanospindle-like  $\text{Cu}_2\text{O}/\text{SMWNTs}$  showed a low detection limit of 200 nM and a high sensitivity of 2.143  $\text{mA cm}^{-2} \text{mM}^{-1}$ .<sup>13</sup> Recently, the record-low detection limit of 5 nM and record-high sensitivity of 12.5  $\text{mA cm}^{-2} \text{mM}^{-1}$  was demonstrated on the nanoporous gold-supported cobalt oxide microelectrode<sup>14</sup>.

Generally, Ag is not as effective as other noble metals (Pt, Pd, Au) in electro-oxidation reaction due to its d-orbital structure and propensity for metal s-d hybridization.<sup>15</sup> In this work, the flower-like Ag NCs was firstly demonstrated as a super-efficient catalyst for glucose sensing. Fig. S13 shows the cyclic voltammograms of flower-like Ag NCs/FTO electrode with and without glucose in 0.1 M NaOH, where the peak  $G_1$ ,  $G_2$ , and  $G_3$  correspond to the formation of  $\text{Ag}(\text{OH})_{\text{ad}}$ ,  $\text{Ag}_2\text{O}$ , and  $\text{AgO}$ , respectively.<sup>16, 17</sup> As reported in the literature, a practical sensitivity can be obtained from the successive amperometric responses under a specific concentration.<sup>14</sup> However, when the concentration of glucose is low, it becomes difficult to collect an effective step-wise amperometric response due to the high noise signal to current density. Taking the nanoporous gold supported cobalt oxide microelectrode as an example,<sup>14</sup> the high sensitivity of 12.5  $\text{mA cm}^{-2} \text{mM}^{-1}$  was calculated based on the glucose concentration of 1  $\mu\text{M}$  rather than its detection limit of 5 nM due to low signal-to-noise ratio in a low glucose concentration. In contrast, the flower-like Ag NCs/FTO electrode can achieve successive amperometric responses with a signal-to-noise ratio of 3 even in a very low glucose concentration from 0.1 to 10 nM (Fig. S14). Supplementary video S1 shows

the amperometric response of the flower-like Ag NCs/FTO electrode upon the successive addition of 0.1 nM glucose into a stirring 0.1 M NaOH solution at an applied potential of 0.95 V. The flower-like Ag NCs/FTO electrode also exhibits a good triple-linear range in three glucose concentration regimes (Fig. S16). The electroactive surface area of metal NCs can be measured by counting the surface sites for hydrogen adsorption based on different electrochemical methods.<sup>18, 19</sup> Here, the equivalent surface of Ag NCs area was determined by the Randle-Sevcik equation in a ferro/ferricyanide redox system:<sup>20</sup>

$$I_p = 2.69 \times 10^5 AD^{1/2}n^{2/3}\nu^{1/2}C^*$$

where  $I_p$  is the peak current,  $A$  is the electroactive area ( $\text{cm}^2$ ),  $n$  is the number of electrons involved in the ferro/ferricyanide redox system ( $n = 1$ ),  $D$  is the diffusion coefficient ( $\text{cm}^2\text{s}^{-1}$ ),  $C^*$  is the bulk concentration of the electroactive species and  $\nu$  is the scan rate ( $\text{Vs}^{-1}$ ). By recording CVs ( $-0.3$  V to  $0.5$  V) in the presence of 10 mM  $\text{K}_3\text{Fe}(\text{CN})_6$  in 0.2 M KCl supporting electrolyte at different scan rates,<sup>21, 22</sup> the peak current  $I_p$  is a linear function of the square root of the potential scan rate (Fig. S15). Based on the slope of  $I_p$  vs  $\nu^{1/2}$ , the equivalent surface area of the flower-like Ag NCs/FTO electrode was determined as  $5.2 \text{ cm}^2$  per unit geometric area in our experiment. Accordingly, this high SA:V Ag NCs/FTO was demonstrated as a highly sensitive electrode for glucose detection with the enhanced electrocatalytic activity per equivalent surface area (sensitivity) of  $4,230 \text{ mA cm}^{-2} \text{ mM}^{-1}$  based on the glucose concentration at the detection limit of 0.1 nM. (Note: the sensitivity of  $2.82 \text{ mA cm}^{-2} \text{ mM}^{-1}$  was obtained at the glucose concentration of 1  $\mu\text{M}$ .) In addition, the mass loading

of flower-like Ag NCs on FTO per geometric area was 8.81  $\mu\text{g}$  measured by inductively coupled plasma atomic emission spectroscopy (Perkin Elmer Optima 8000). Therefore, the specific surface area of 59  $\text{m}^2/\text{g}$  can be obtained for the flower-like Ag NCs. It also demonstrated the enhanced electrocatalytic activity per unit mass of  $2.496 \times 10^9 \text{ mA g}^{-1} \text{ mM}^{-1}$  at the glucose concentration of 0.1  $\text{nM}$ .

## References

- 1 P. L. Redmond, A. J. Hallock and L. E. Brus, *Nano Lett.*, 2005, **5**, 131-135.
- 2 T. Bligaard, J. Nørskov, S. Dahl, J. Matthiesen, C. Christensen and J. Sehested, *J. Catal.*, 2004, **224**, 206-217.
- 3 T. Fujita, P. Guan, K. McKenna, X. Lang, A. Hirata, L. Zhang, T. Tokunaga, S. Arai, Y. Yamamoto and N. Tanaka, *Nature Mater.*, 2012, **11**, 775-780.
- 4 Y. Xiong and Y. Xia, *Adv. Mater.*, 2007, **19**, 3385-3391.
- 5 Y. Xiong, J. M. McLellan, J. Chen, Y. Yin, Z.-Y. Li and Y. Xia, *J. Am. Chem. Soc.*, 2005, **127**, 17118-17127.
- 6 R. Long, S. Zhou, B. J. Wiley and Y. Xiong, *Chem. Soc. Rev.*, 2014, **43**, 6288-6310.
- 7 K.-S. Choi, *Dalton T.*, 2008, 5432-5438.
- 8 Q. Zhang, N. Li, J. Goebel, Z. Lu and Y. Yin, *J. Am. Chem. Soc.*, 2011, **133**, 18931-18939.
- 9 L. Hong, Q. Li, H. Lin and Y. Li, *Mater. Res. Bull.*, 2009, **44**, 1201-1204.

- 10 A. Berná, J. M. Delgado, J. M. Orts, A. Rodes and J. M. Feliu, *Electrochim. Acta*, 2008, **53**, 2309-2321.
- 11 G. Wang, X. He, L. Wang, A. Gu, Y. Huang, B. Fang, B. Geng and X. Zhang, *Microchimica Acta*, 2013, **180**, 161-186.
- 12 Y. Y. Song, D. Zhang, W. Gao and X. H. Xia, *Chemistry—A European Journal*, 2005, **11**, 2177-2182.
- 13 X. Zhou, H. Nie, Z. Yao, Y. Dong, Z. Yang and S. Huang, *Sensor Actuat. B: Chem.*, 2012, **168**, 1-7.
- 14 X.-Y. Lang, H.-Y. Fu, C. Hou, G.-F. Han, P. Yang, Y.-B. Liu and Q. Jiang, *Nat. Commun.*, 2013, **4**.
- 15 J. K. Nørskov, F. Abild-Pedersen, F. Studt and T. Bligaard, *P. Natl. Acad. Sci. Usa.*, 2011, **108**, 937-943.
- 16 M. K. Kundu, M. Sadhukhan and S. Barman, *J. Mater. Chem. B.*, 2015, **3**, 1289-1300.
- 17 S. S. A. El Rehim, H. H. Hassan, M. A. Ibrahim and M. A. Amin, *Monatshefte für Chemie/Chemical Monthly*, 1998, **129**, 1103-1117.
- 18 N. Tian, Z.-Y. Zhou, S.-G. Sun, Y. Ding and Z. L. Wang, *Science*, 2007, **316**, 732-735.
- 19 J. Ryu, K. Kim, H.-S. Kim, H. T. Hahn and D. Lashmore, *Biosens. Bioelectron.*, 2010, **26**, 602-607.
- 20 A. J. Bard, L. R. Faulkner, J. Leddy and C. G. Zoski, *Electrochemical methods: fundamentals and applications*, Wiley New York, 1980.

- 21 L. Yuan, M. Yang, F. Qu, G. Shen and R. Yu, *Electrochim. Acta*, 2008, **53**, 3559-3565.
- 22 F. Manea, *Modern Electrochemical Methods in Nano, Surface and Corrosion Science*, InTech, 2014.